HHS Public Access

Author manuscript

Cell Rep. Author manuscript; available in PMC 2019 January 03.

Published in final edited form as:

Cell Rep. 2018 November 20; 25(8): 2017–2026.e3. doi:10.1016/j.celrep.2018.10.089.

Synaptic Convergence Patterns onto Retinal Ganglion Cells Are Preserved despite Topographic Variation in Pre- and Postsynaptic Territories

Wan-Qing Yu[1], **Rana N. El-Danaf**[2], **Haruhisa Okawa**[1], **Justin M. Pacholec**[1], **Ulf Matti**[3,8], **Karin Schwarz**[3], **Benjamin Odermatt**[4], **Felice A. Dunn**[5], **Leon Lagnado**[6], **Frank Schmitz**[3], **Andrew D. Huberman**[2,7], and **Rachel O.L. Wong**[1,9,*]

[1]Department of Biological Structure, University of Washington, Seattle, WA 98195, USA

[2]Department of Neurobiology, Stanford University School of Medicine, Stanford, CA 94305, USA

[3]Department of Neuroanatomy, Medical School Homburg/Saar, Institute for Anatomy and Cell Biology, Saarland University, 66421 Homburg/Saar, Germany

[4]Institute of Anatomy, University of Bonn, 53115 Bonn, Germany

[5]Department of Ophthalmology, University of California, San Francisco, San Francisco, CA 94143, USA

[6]School of Life Sciences, University of Sussex, Brighton BN1 9QG, UK

[7]Departments of Neurobiology and Ophthalmology, Stanford Neurosciences Institute, and BioX, Stanford University School of Medicine, Stanford, CA 94305, USA

[8]Present address: European Molecular Biology Laboratory, 69117 Heidelberg, Germany

[9]Lead Contact

SUMMARY

Sensory processing can be tuned by a neuron's integration area, the types of inputs, and the proportion and number of connections with those inputs. Integration areas often vary topographically to sample space differentially across regions. Here, we highlight two visual circuits in which topographic changes in the postsynaptic retinal ganglion cell (RGC) dendritic territories and their presynaptic bipolar cell (BC) axonal territories are either matched or unmatched. Despite this difference, in both circuits, the proportion of inputs from each BC type,

*Correspondence: wongr2@uw.edu.

AUTHOR CONTRIBUTIONS

Conceptualization, W.-Q.Y., H.O., and R.O.L.W.; Methodology, W.-Q.Y., H.O., and R.O.L.W.; Software, W.-Q.Y., H.O., and J.M.P.; Investigation, W.-Q.Y., R.N.E.-D., H.O., and J.M.P.; Resources, U.M., K.S., B.O., F.A.D., L.L., F.S., A.D.H., and R.O.L.W.; Writing - Original Draft, W.-Q.Y. and R.O.L.W.; Writing - Review & Editing, W.-Q.Y., R.N.E.-D., H.O., B.O., F.A.D., L.L., F.S., A.D.H., and R.O.L.W.

DECLARATION OF INTERESTS

The authors declare no competing interests.

SUPPLEMENTAL INFORMATION

Supplemental Information includes four figures and can be found with this article online at https://doi.org/10.1016/j.celrep.2018.10.089.

i.e., synaptic convergence between specific BCs and RGCs, remained constant across varying dendritic territory sizes. Furthermore, synapse density between BCs and RGCs was invariant across topography. Our results demonstrate a wiring design, likely engaging homotypic axonal tiling of BCs, that ensures consistency in synaptic convergence between specific BC types onto their target RGCs while enabling independent regulation of pre- and post-synaptic territory sizes and synapse number between cell pairs.

Graphical Abstract

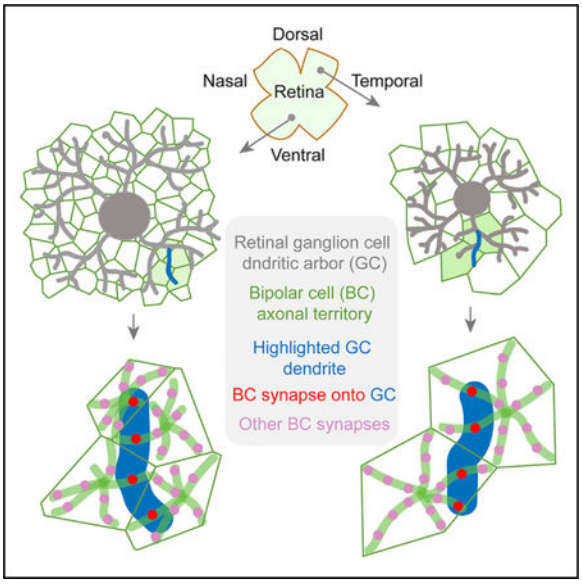

In Brief

Yu et al. show that the density of excitatory synapses on retinal output neurons is invariant of retinal location, even though connectivity between pre- and postsynaptic cell pairs can vary. These results have implications for understanding topographic variations in processing of visual stimuli and for understanding consistency of CNS wiring diagrams.

INTRODUCTION

The sensory integration area of a neuron is defined by its spatial receptive field, which often corresponds to the dendritic territory of the neuron. Other properties of the physiological receptive field, such as its temporal dynamics, are shaped in part by the combination of presynaptic partner types and by the wiring patterns with these partners (Awatramani and Slaughter, 2000; Niell, 2015; Roska and Werblin, 2001). The presynaptic cells themselves also have receptive fields, which in some circuits form a substructure composed of ‘‘subunits’’ within the postsynaptic cell’s integration area (Demb et al., 2001; Freeman et al., 2015; Rust et al., 2005; Schwartz et al., 2012). These functional sub-units provide finer spatial sampling that is engaged in the detection of additional stimulus features (Gollisch, 2013; Schwartz and Rieke, 2011).

The spatial receptive fields of sensory neurons have been found to modify in size systematically across the sensory surface. For example, receptive fields and corresponding dendritic territories of many retinal ganglion cell (RGC) types are relatively more compact at locations that are involved in high acuity vision, such as the fovea (Dacey, 1993; Hammond, 1974; Polyak, 1941). Likewise, neurons in the somatosensory cortex with the smallest receptive fields show enhanced discrimination between adjacent points of contact (Kaas et al., 1979; Knibestöl and Vallbo, 1970). These receptive field variations reflect diverse spatial sampling needs across the sensory field. Such topographic variation within a given neuronal cell type raises the question of whether topological changes in the cell's spatial receptive field are accompanied by similar alterations in its subunits. An answer to this question will reveal whether receptive field subunits are regulated separately or together with that of the postsynaptic neuron. To answer this question, we thus turn to the vertebrate retina, where the clearest examples of receptive fields with functionally defined subunits can be found.

Previous recordings from RGCs revealed the presence of nonlinear computation at a spatial scale finer than that of the RGC's receptive field center (Demb et al., 1999; Enroth-Cugell and Robson, 1966; Hochstein and Shapley, 1976; Petrusca et al., 2007; Stone and Pinto, 1993). Nonlinear subunits have been found to permit RGCs to detect fine texture within its spatial receptive field center (Demb et al., 2001; Hochstein and Shapley, 1976; Schwartz et al., 2012) to facilitate detection of the movement of an object in the presence of a moving background (Olveczky et al., 2007) and to generate the response to looming stimuli (Münch et al., 2009). Studies using different size gratings or textured stimuli show that, in some RGCs, the size of the sub-unit corresponds to the size of the receptive field of the bipolar cell (BC), providing the major drive to the recorded RGC, implicating that, for these RGCs, the BC is the structural correlate of the nonlinear subunit (Crook et al., 2008; Demb et al., 2001; Schwartz et al., 2012). Using the mouse retina, where previous work has shown that dendritic arbors of some RGC types exhibit topographic variations in size (Bleckert et al., 2014; El-Danaf and Huberman, 2018; Hughes et al., 2013; Warwick et al., 2018; Zhang et al., 2012), we asked whether BCs also vary in size across the retina. We then asked: do the changes in the BCs vary together with that of their partner RGCs? To obtain a measure of BC size, we quantified the axonal territory area of the BC, which is proportional to the areas of its dendritic arbor and its corresponding receptive field (Berntson and Taylor, 2000; Dunn and Wong, 2012; Zhang and Wu, 2009).

Mouse RGCs, like other CNS neurons (Berck et al., 2016; Callaway, 2002; Fişek and Wilson, 2014), receive input from more than one type of excitatory neuron i.e., each RGC type is contacted by more than one BC type (Dunn and Wong, 2014). Moreover, connectivity with different BC types appears stereotypic (Morgan et al., 2011). Such stereotyped synaptic convergence begs the following additional questions: is connectivity maintained with the same BC types at different retinal locations, and if so, is the proportion of synapses from each BC partner type (synaptic convergence ratio) maintained? The answers will provide insight into whether the balance of synaptic drive from distinct BC input types is maintained as the postsynaptic RGC's receptive field expands or shrinks.

To ascertain the topographic relationship between the RGC dendritic territories and BC axonal territories, we chose two types of mouse RGCs, OFF-sustained (OFF-S) and OFF-

transient (OFF-T) alpha cells for our analysis. Alpha and alpha-like RGCs are found in all vertebrate species and are generally found to be motion sensitive and non-direction selective (Sanes and Masland, 2015). These ganglion cell types have previously been suggested to show systematic variations in their dendritic field size across the retina (Bleckert et al., 2014). The gradients in cell arbor size occur along different axes for these two RGC types. Both types are depolarized by light decrement (light-OFF), which suggests that they receive direct excitatory input from glutamatergic OFF cone BCs. There are five to six types of OFF cone BCs whose axonal terminals stratify at different depths of the inner plexiform layer (IPL) (Euler et al., 2014; Tsukamoto and Omi, 2014). Because of their distinct dendritic stratification patterns in the IPL, OFF-S and OFF-T alpha RGCs are presumed to connect differently to the OFF cone BCs (Bleckert et al., 2014; van Wyk et al., 2009). However, these synaptic patterns have not been identified or mapped systematically for the OFF-S and OFF-T RGCs across retinal locations. We thus determined the BC connectivity patterns of these RGC types across the retina using biolistic transfection methods to mark glutamatergic postsynaptic sites (PSD95). The dendritic arbors of the RGCs were visualized in the background of the OFF BC types, identified either by immunostamning or in GFP-expressing transgenic mouse lines. Comparison of the BC-RGC connectivity maps revealed uncorrelated topographic changes in axonal territory sizes among some BC types and differences in the degree of BC axonal and RGC dendritic territory scaling involving the two RGC types. Regardless of the axonal and dendritic arbor size distributions, the synaptic convergence ratios of BC synapses of the populations of each BC type were found to remain constant for both RGC types across the retina. However, some, but not all, of the BC types demonstrated topographic changes in axonal arbor size, and these variations did not always scale along the same retinal axis as the dendritic arbors of their postsynaptic ganglion cell.

RESULTS

Distinct Topographic Distributions of Two Types of OFF Alpha RGCs

OFF-S alpha RGCs labeled in *Thy1-YFP-H* transgenic mice appear to display a nasal to temporal gradient in their dendritic arbor size (Bleckert et al., 2014). We quantified here the dendritic arbor sizes of the OFF-S RGCs along the nasal-temporal axis after biolistic transfection with plasmids encoding a fluorescent protein to label cells and their glutamatergic postsynaptic sites. Examples of OFF-S RGCs in the nasal and temporal retina labeled biolistically are shown in Figures 1A and 1B. The dendritic arbor sizes obtained using this approach were within the size range of arbors at the same retinal eccentricities, obtained by conventional intracellularly dye filling (Figures 1C and 1D). The dendritic field diameter of the OFF-S alpha RGCs decreased from nasal to temporal retina (Figures 1C and 1D; linear regression: $y = \alpha + \beta x$; $\beta = -56.00$; $p = 0.006$; $r^2 = 0.26$).

Previously, we showed that OFF-T alpha RGCs demonstrate a small change in cell density from dorsal to ventral retina (Bleckert et al., 2014). Because RGC dendritic arbor size scales inversely with their cell density (Wässle and Boycott, 1991), we expected that OFF-T RGCs would show a corresponding shallow gradient in their arbor size. We measured directly the arbor sizes of OFF-T alpha RGCs using biolistics and by dye-filling GFP-expressing OFF-T RGCs (Figures 1E–1H) in CB2-GFP mice (Huberman et al., 2008). We confirmed a small

but significant decrease along the dorsal-ventral axis (Figure 1H; linear regression: $y = \alpha + \beta x$; $\beta = -29.41$; $p = 0.006$; $r^2 = 0.06$) for the pooled data. Thus, both OFF-S and OFF-T alpha RGCs show dendritic arbor size gradients across the retina, which occur along different retinal axes: OFF-S varies along the nasal-temporal axis whereas OFF-T varies along the dorsal-nasal axis.

Glutamatergic Synapse Densities on OFF Alpha RGC Dendritic Arbors Are Topographically Invariant

The topographic variation in OFF alpha RGC dendritic arbor size prompted us to ask whether the density of excitatory post-synaptic sites on the dendrites of the OFF-S and OFF-T RGCs also change with retinal location. We thus quantified the density of excitatory postsynaptic sites on OFF alpha RGCs that were biolistically colabeled with BFP and PSD95-RFP (Figures 1I–1P). PSD95-RFP puncta appeared relatively evenly distributed on both OFF-S and OFF-T alpha RGC dendrites (Figures 1I–1L). Overall, OFF-T alpha RGCs had a slightly higher PSD95 density compared to OFF-S alpha RGCs (OFF-T alpha RGCs: 0.41 ± 0.01 [number of puncta/μm]; OFF-S alpha RGCs:0.34 ± 0.01 [number/μm]; $p = 0.001$). For either RGC type, we found no significant difference in PSD95 density between retinal locations where arbor sizes differed (Figures 1M and 1O; OFF-S: $p = 0.884$; OFF-T: $p = 0.352$). PSD95 density was invariant of the dendritic arbor size of the OFF alpha RGCs (Figures 1N and 1P).

Topographic Variations in BC Axonal Territories Are Not Consistent across BC Types

To determine whether the potential presynaptic partners of these RGCs also showed topographic variation, we examined the axonal territories of BCs. We measured the axonal territories of various OFF BC types (T1, T2, T3a, and T4 OFF BCs) that could be presynaptic partners of the OFF alpha RGCs and compared these measures at different locations. OFF bipolar cells were labeled in retinas from *Vsx1-cerulean* transgenic mice, of which there are two lines: *Vsx1-cerulean1* (line 1) shows sparse labeling of types 1–4 (T1–4) BCs (Della Santina et al., 2016; Hoon et al., 2015), whereas the majority of bipolar cells labeled in *Vsx1-cerulean2* (line 2; see STAR Methods) are T1 BCs, which do not immunolabel for synaptotagmin-2 (Syt2) (Fox and Sanes, 2007), a marker for T2 BCs (Figure 2A). Because T2 BCs are very sparse in the *Vsx1-cerulean1* line, we identified the T2 population by imunostaining for Syt2. Additionally, populations of T4 BCs were visualized using the *5HTR2a-GFP* line. Axonal terminal sizes of the T1, T3a, and T4 OFF BCs were obtained directly using transgenic mouse lines (Figures 2A, 2C, and 2D). For T2 BCs immunolabeled with Syt2, we inferred their axonal territory size from their cell distribution because the arbors of neighboring cells could not be separated (Figure 2B). This was achieved by generating and measuring the sizes of the Voronoi domains based on the spatial distribution of the Syt2-labeled axonal stalks (Figure 2B). The Voronoi domains are a reasonable estimate (Figure S1) of the axon territories because the axon terminals of each BC type do not overlap, i.e., they tile (Wä ssle et al., 2009).

There were three main observations. First, some, but not all, BC types exhibited topographic variations in axonal territory size (Figures 2E–2H). Among the four BC types we examined, only T1 BCs showed a relatively constant axon terminal size across the retina (Figure 2E;

Kruskal-Wallis test; p = 0.790). Topographic variations in axonal size differed in extent among the other three BCs types (Figures 2B–2D; Kruskal-Wallis test; T2: p = 0.038; T3a: p = 0.006; T4: p < 0.001). Second, for T2, T3a, and T4 BCs, their axon terminal sizes are relatively smaller in ventral compared to dorsal retina. Third, comparison of Figures 1 and 2 suggests that topographic variation in dendritic arbor sizes in RGCs and in axonal territory sizes in OFF BCs could be matched or unmatched, depending on which BC types connect with which RGC types.

OFF BCs Maintain Their Stereotypic Synaptic Convergence onto OFF RGCs across the Retina

Because both RGC dendritic arbors and BC axonal territories can vary in size across the retina, it is possible that the synaptic convergence ratio (i.e., the proportion of synapses) of the different BC partner types with their postsynaptic RGC type may also alter with location. To determine whether bipolar cell convergence onto the OFF alpha RGCs is invariant with retinal location, we first identified the OFF BC types that synapse with each of the two OFF alpha cell types. We then compared the BC convergence ratio onto OFF-S and OFF-T alpha RGCs at two locations of the retina, where each RGC type exhibits different dendritic arbor sizes (Figure 3). RGCs were labeled with a plasmid encoding BFP and PSD95-RFP. T1 and T4 BCs were identified using transgenic lines, and T2 and T3a BCs were labeled by Syt2 and HCN4 (Mataruga et al., 2007), respectively.

We found that each ganglion cell type has distinct convergence ratios from the OFF BC types. OFF-S alpha RGCs received the majority of their glutamatergic synapses from T2, followed by T3a, T1, and T4 BCs (Figures 3A and3C). This is apparent from the connectivity maps provided in Figure 3A. The proportions of synapses from each BC partner type were 50.6% ± 1.3% from T2, 6.4% ± 2.3% from T3a, 4.4% ± 1.1% from T1, and 3.7% ± 0.6% from T4 BCs. In contrast, OFF-T alpha RGCs were largely connected to T3a, followed by T4, T2, and T1 BCs (Figures 3B and 3C). The proportions of synapses from each BC partner type were 39.8% ± 1.4% (T3a), 17.6% ± 0.9% (T4), 2.1% ± 0.5% (T2), and 0.07% ± 0.07% (T1; Figure 3C). Note that the sum of the BC inputs here falls short of 100% because some inputs are provided by yet undefined cell types (see Discussion). Nevertheless, our results thus far demonstrate that the two OFF alpha RGCs receive stereotypic and distinct combinations of excitatory input from separate OFF BC types.

What factors could give rise to the different patterns of BC connectivity with OFF-S and OFF-T alpha RGCs? We explored whether the extent of axon-dendrite overlap (Peters and Feldman, 1976) is a major contributing factor. We also asked whether mechanisms are required to limit partners whose processes are in close proximity (Williams et al., 2010; Zhang et al., 2017; Zipursky and Sanes, 2010). We thus considered two scenarios: first, we examined synaptic contacts between an individual BC type and the two OFF alpha RGCs and, second, we examined connectivity between a single OFF alpha RGC type and two BC types whose axon terminals arborize within the depth of the RGC’s dendritic arbor. We discovered that co-stratification increases the likelihood of (Figures S2A–S2C), but does not guarantee, connectivity between a pair of OFF alpha RGCs and a BC type (Figures S2D and S2E). Although the dendrites of OFF-S alpha RGCs intermingled with axon terminals of

both T1 and T2 BCs at the same depth, OFF-S alpha RGCs form more synaptic contacts with T2 than with T1 BCs (Figures S2D and S2E; for quantification, see Figure 3C). RGC dendritic arbors stratify prior to the differentiation of BCs (Coombs et al., 2007; Morgan et al., 2006). Our observations here thus suggest that BC axons use cues apart from dendritic lamination of RGCs to target these partners.

Do BC convergence ratios vary across the retina? We found that, irrespective of RGC or BC arbor size, the BC convergence pattern of each OFF alpha RGC type remained the same (Figure 3C). Moreover, there is no significant correlation between the percentage of synapses formed with the major (Figure S3A) or minor (Figure S3B) BC partner type and the RGC dendritic arlbor size. Thus, the pattern of BC synaptic convergence onto the OFF alpha RGCs is maintained despite topographic changes in the size of BC or RGC arbors.

BC Ribbon Number Increases Systematically with Axonal Terminal Volume

How do OFF alpha RGCs maintain their stereotypic connectivity patterns with different presynaptic OFF BC types across the retina? One possible explanation is that each BC population forms a constant density of synapses across the retina. If so, we predict that the number of presynaptic sites (ribbons) of a BC type scales with their axon terminal volume. We thus quantified the number of ribbons within individual BC axon terminals (Figure 4) upon crossing *Ribeye-ribeye-tagRFP* mice (see STAR Methods) with either *Vsx1-cerulean1*, *Vsx1-cerulean2*, or *5HTR2a-EGFP* mice. As reported previously, OFF BCs are labeled sparsely *Vsx1-cerulean1* mice. Although there are very few T2 BCs in the retinas of *vsx1-cerulean1* mice, this cell type was more frequently observed in offspring of these mice bred with *Ribeye-ribeye-tagRFP* mice. We confirmed the identity of isolated T2 or T3a BCs by immunolabeling for Syt2 or HCN4, respectively. For all BC types, we found the ribbon density per BC to be consistent across retinal location (Figure 4B; T1: $p = 0.573$; T2: $p = 0.282$; T3a: $p = 0.534$; T4: $p = 0.132$). Rib-bon number and axon terminal volume of each BC type clearly show a positive correlation (Figure 4C). Our data therefore suggest that the convergence ratio of the different BC types onto the OFF alpha RGCs may be the same across the retina because the density of synapses provided by each BC type is invariant with retinal location, despite changes in the size of their axonal terminals.

DISCUSSION

RGC connectivity with BCs has been ascertained from serial EM reconstructions (Dunn and Wong, 2014; Helmstaedter et al., 2013), using synapse-specific markers in light microscopy and by electrophysiological recordings from BC and RGC pairs (Morgan et al., 2011; Schwartz et al., 2012; Tien et al., 2017). Here, we used synaptic markers to assess and map the connectivity of OFF alpha RGCs and OFF BCs across the retina. At least 40%–50% of the total synapses on OFF-S and OFF-T alpha RGCs are made with a single OFF BC type (Figure S4). As in a previous study (Neumann et al., 2016), we found that T2 BCs provide the major BC input to OFF-S alpha RGC. In contrast, T1 BCs do not appear to be a major partner of the OFF-S, as suggested previously by an electron microscopy (EM) study based on apposition of cell membranes (Helmstaedter et al., 2013). This discrepancy may be because the RGC type identified in Helmstaedter et al. (2013) may not be an OFF-S RGC

(Bae et al., 2018). Our current findings are consistent with the possibility that a non-conventional glutamatergic neuron, the GlMMIs, provides significant synaptic input to the OFF-S alpha cells (Della Santina et al., 2016). Putative OFF-T alpha RGCs (Bae et al., 2018) identified from the serial EM reconstructions are contacted largely by T3a, T3b, and T4 BCs compared to T2 BCs (Helmstaedter et al., 2013). This is consistent with our observations here, except that we could not assess the connectivity of T3b BCs because their axon terminals cannot yet be visualized using cell-specific markers and light microscopy. T3b could, therefore, account for some of the remaining unidentified synaptic inputs on the OFF-T RGC (Figure S4C). In addition, VGlut3 amacrine cells may also provide significant input onto the OFF-T RGC (Lee et al., 2016).

Previous studies suggest that OFF alpha RGCs show distinct topographic variations in their dendritic arbor size (Figure S4A). Here, we confirmed that OFF-S alpha RGCs possess a nasal-temporal decrease in dendritic arbor size, whereas OFF-T alpha RGCs display a decrease along the dorsal-ventral axis (Figure S4A). We found that three of the four types of OFF BCs we examined (T2, T3a, and T4) exhibited relatively larger axon terminals in dorsal compared to ventral retina (Figure S4B). In contrast, T1 axonal arbor sizes were unchanged across the retina. Therefore, OFF BC types, like the OFF alpha RGCs, show differences in topographic variation in the size of their arbors. We found that OFF-T alpha RGCs and T3a and T4 BCs, their major BC input types, vary along the same retinal axis. The relatively smaller sizes of the OFF-T RGC and their major BC partners in the ventral retina would ensure better spatial resolution for the detection, by these RGCs, of objects looming above the animal (Münch et al., 2009). In contrast, OFF-S alpha RGC dendritic and T2 BC axonal arbors do not vary in parallel and in fact alter along different retinal axes. Such uncoordinated changes were also apparent for ON-S alpha RGCs and their major input, the T6 BCs (Bleckert et al., 2014). Such uncorrelated topographic changes in BC and RGC arbors suggest that, for some RGCs, BC receptive field subunit sizes are regulated separately from that of the RGC spatial receptive field. Moreover, because the number of BC output sites (ribbons) is proportional to the size of the BC axonal arbor, pairwise BC-RGC connectivity could alter with retinal location. Such variation in connectivity between individual BCs and their target RGCs could provide a means for fine adjustments of receptive field subunits (Schwartz et al., 2012). Future experiments are, however, needed to uncover the functional benefits for matching or non-matching topographic changes between RGCs and their presynaptic BC partners.

Despite non-matching changes in BC and RGC territories in some RGC-BC circuits, the stereotypic synaptic convergence pattern between BCs and RGCs appears preserved regardless of retinal location. However, because the axonal arbors of neighboring BCs of the same type tile (Wässle et al., 2009) and BC ribbon density are constant, each BC type provides a consistent coverage of the retinal area and a constant density of output synapses from its population despite changes in the terminal sizes of individual BCs. Thus, along any length of RGC dendrite, the density of synapses formed by each BC type is unchanged, even though the number of synapses between a BC-RGC pair can vary (Figure S4D). Interestingly, recent EM reconstructions suggest that the dendritic density of an individual RGC type is uniform (Bae et al., 2018). The spatial arrangements of the populations of BC

axonal territories and RGC dendritic arbors may thus both contribute to ensuring an unchanging synapse density provided by each BC type to its target RGC population.

Although our current work has focused on the contributions of BC connections to the RGC spatial receptive field, how temporal properties of RGC receptive fields vary with retinal location also requires attention. Previous work suggested there is matching of the temporal responses to light of the excitatory interneurons and their postsynaptic RGCs (Awatramani and Slaughter, 2000; Della Santina et al., 2016; Franke et al., 2017). However, stimulation of an individual BC can result in different temporal responses of distinct postsynaptic RGC partners (Asari and Meister, 2012). Moreover, differential glycinergic inhibition onto OFF-T alpha RGCs or their presynaptic inputs have recently been shown to modify the temporal response of these RGCs along the dorsalventral axis (Warwick et al., 2018). This inhibition is provided by the primary rod pathway and does not involve the cone pathway. Preserving the synaptic convergence patterns of BC-RGCs may not contribute to defining the ‘‘transient’’ or ‘‘sustained’’ nature of the RGC output. Stereotypic BC-RGC connectivity patterns, however, are likely to be important for shaping other output properties of RGCs, e.g., synaptic gain or signal-to-noise ratios. Notably, maintaining the proportion of input types across the RGC dendritic arbor would ensure properties, such as the input signal-to-noise ratio, at the majority of synapses across the arbor. In contrast, changes in the proportion of input types would change the balance of information from each BC channel, perhaps changing functional properties of RGCs across retinal location. Future work comparing the properties of synaptic transmission from an individual BC or BC type to different postsynaptic RGC types will provide insight into the role(s) these interneurons play in generating receptive fields that help define the visual processing features of their disparate RGC partners.

STAR★METHODS

KEY RESOURCES TABLE

REAGENT or RESOURCE	SOURCE	IDENTIFIER
Antibodies		
Mouse monoclonal anti-synaptotagmin II	Zebrafish International Resource	Cat# znp-1; RRID: AB_10013783
Rabbit polyclonal anti-HCN4	Alomone Labs	Cat# APC-052, RRID:AB_2039906
Chicken polyclonal anti-GFP	Abcam	Cat# ab13970, RRID:AB_300798
Mouse monoclonal anti-myc	DSHB	Cat# 9E 10, RRID:AB_2266850
Donkey polyclonal anti-chicken IgY, Alexa Fluor 488	Jackson ImmunoResearch Labs	Cat# 703-545-155, RRID: AB_2340375
Donkey polyclonal anti-rabbit IgG, Alexa Fluor 647	Jackson ImmunoResearch Labs	Cat# 711-605-152, RRID: AB_2492288
Goat anti-mouse IgG2a, Alexa Fluor 647	Jackson ImmunoResearch Labs	Cat# 115-605-206, RRID: AB_2338917
Goat anti-mouse IgG1, DyLight 405	Jackson ImmunoResearch Labs	Cat# 115-477-185, RRID: AB_2632529
Chemicals, Peptides, and Recombinant Proteins		
Alexa Fluor 555 hydrizide	Invitrogen	Cat# A20501MP
Normal Donkey Serum	Sigma-Aldrich	Cat# D9663
Vectashield	Vector Laboratories	Cat# H-1000, RRID: AB_2336789
Gold Particles/micro carriers (1.6 μm diameter)	Bio-Rad	Cat# 165-2264
Experimental Models: Organisms/Strains		
Mouse model: Vsx1-cerulean2	This paper	N/A
Mouse model: Vsx1-cerulean1	(Hoon et al., 2015)	N/A
Mouse model: Ribeye-ribeye-tagRFP	This paper	N/A
Mouse model: CB2-GFP	(Huberman et al., 2008)	RRID:MMRRC_000283-MU
Mouse model: 5HTR2a-EGFP	(Lu et al., 2009)	RRID:MMRRC_010915-UCD
Mouse model: Grm6-tdTomato	(Kerschensteiner et al., 2009)	N/A
Mouse model: Gus8.4-GFP	The Jackson Laboratory	RRID: IMSR_JAX:026704
Recombinant DNA		
Plasmid: pCMV-CFP	(Morgan et al., 2011)	N/A
Plasmid: pCMV-tagBFP2-myc	This paper (Modified from pEGFP-N1 from Clonetech)	N/A
Plasmid: pCMV-PSD95-tagRFP	This paper (Modified from pCMV-PSD95-YFP)	N/A
Plasmid: pCMV-PSD95-YFP	A.M.Craig, University of British Columbia (Morgan et al., 2008)	N/A
Software and Algorithms		
ImageJ	NIH	https://imagej.nih.gov/ij/, RRID: SCR_003070

REAGENT or RESOURCE	SOURCE	IDENTIFIER
Amira	Thermo-Fisher Scientific	https://www.fei.com/software/amira-avizo/, RRID: SCR_014305
Imaris	Bitplane	http://www.bitplane.com/, RRID: SCR_007370
MATLAB	MathWorks	https://www.mathworks.com/products/matlab.html, RRID: SCR_001622
R	R Core Team	https://www.r-project.org/, RRID:SCR_001905

CONTACT FOR REAGENT AND RESOURCE SHARING

Further information and requests for resources and reagents should be directed to and will be fulfilled by the Lead Contact, Rachel O.L. Wong (wongr2@uw.edu).

EXPERIMENTAL MODEL AND SUBJECT DETAILS

Mice—All experiments were conducted following animal protocols approved by the Institutional Animal Care and Use Committee at University of Washington and Stanford University School of Medicine. All procedures in these protocols are in compliance with the National Institute of Health Guidelines for the Care and Use of Laboratory Animals. Adult mice ranging in age between postnatal days (P) 30–60, of either sex were used. CB2-GFP mouse line was used to target OFF-T alpha RGCs (Huberman et al., 2008). Three different transgenic mouse lines were used to target specific fluorescently-labeled BC subtypes: *vsx1-cerulean1* (Hoon et al., 2015), *vsx1-cerulean2* and *5HTR2a-EGFP* (Lu et al., 2009). *Vsx1-cerulean2* mice were screened from the same pool of potential founder lines as *vsx1-cerulean1*. Whereas Types 1–4 OFF BCs are found sparsely labeled in *vsx1-cerulean1* mice, the majority of labeled OFF BC cells in *vsx1-cerulean2* retinas are Type 1 BCs. Patches of T4 BCs were expressed in *5HTR2a-EGFP* (Lu et al., 2009). *Ribeye-ribeye-tagRFP* mice were generated to visualize ribbons in the retina. Briefly, these mice were produced by pronucleus injection of a DNA construct that contained the mouse Ribeye promotor placed upstream of an expression cassette that encoded for full-length rat Ribeye fused in frame to tagRFP-T (Shaner et al., 2008). Pronucleus injection which was performed by Frank Zimmermann/Sascha Dlugosz (IBF; University of Heidelberg). Positive founder mice were identified by genomic PCR using appropriate primer pairs. We crossed *Ribeye-ribeye-tagRFP* mice with either BC lines mentioned above to quantify ribbon numbers in individual BC axon terminals.

METHOD DETAILS

Tissue preparation—Mice were deeply euthanized with isoflurane followed by decapitation, and their eyes were enucleated. For immunohistochemistry and biolistic transfection, the eyes were then transferred to oxygenated mouse artificial cerebrospinal fluid (mACSF, pH 7.4) containing (in μm) 119 NaCl, 2.5 KCl, 2.5 $CaCl_2$, 1.3 $MgCl_2$, 1 NaH_2PO_4, 11 glucose and 20 HEPES at room temperature. After removing the anterior eye and vitreous, a deep cut was made on ventral side to mark the orientation of the eyes (Wei et al., 2010). The retina was isolated from the eyecup and mounted on a nitrocellulose membrane disc (Millipore) with retinal ganglion cell side up. The retinas were subsequently

fixed for 15–20 minutes in 4% paraformaldehyde in mACSF. For intracellular dye-fill, the dorsal pole of the left and right eyes were marked before removing them from the animal, using waterproof color markers thus ensuring that knowledge about retinal location was preserved (Wei et al., 2010). Retinas were isolated and kept in oxygenated (95% O_2/5% CO_2) $NaHCO_3$ (23 μm) containing Ames' medium (Sigma-Aldrich).

Immunohistochemistry—The retinas were pre-incubated in blocking solutions containing 5% normal donkey serum for 2 hours under room temperature. Then, they were incubated in primary antibodies for 3 nights at 4°C. Secondary antibodies were antiisotypic DyLight (1:1000, Jackson ImmunoResearch) or Alexa conjugates (1:1000, Invitrogen). Primary antibodies used in this study were: anti-GFP (chicken polyclonal, 1:1000, Abcam), anti-Synaptotagmin-2 (mouse monoclonal, 1:1000, znp-1, Zebrafish International Resource Center), anti-HCN4 (rabbit polyclonal, 1:500, Alomone Labs) and anti-myc (mouse IgG1, 1:1000, deposited to the DSHB by Bishop, J.M.).

Biolistic transfection—Gold particles (1.6 μm diameter, 12.5 mg, Bio-Rad) were coated with DNA plasmids encoding cerulean or BFP-myc (24 mg), PSD95-YFP or PSD95-RFP (12 mg) under the control of the cytomegalovirus (CMV) promoter. The particles were delivered to retinal ganglion cells in whole-mount retinas using a Helios gene gun (40 psi, Bio-Rad). Transfected retinas were kept overnight in mACSF in a humid, oxygenated chamber at 33°C.

Intracellular dye-filling—Labeling of individual RGCs was performed using a previously described protocol (Beier et al., 2013; Cruz-Martı´n et al., 2014; Dhande et al., 2013; El-Danaf and Huberman, 2015). The fluorescent RGC somas were localized using differential interference contrast (DIC) and epifuorescence microscopy. RGCs were targeted with borosilicate glass electrodes (Sutter Instruments; 15–20 MU) containing Alexa Fluor 555 hydrizide dye (10 mM in 200 mM KCl; Invitrogen), and were completely filled by applying hyperpolarizing current pulses ranging between 0.1– 0.9 nA for ≤ 1 minute.

Image acquisition—Image acquisition protocols for dye-filled retinas were previously described (El-Danaf and Huberman, 2015). Individual RGCs were imaged using a laser scanning confocal microscope (Zeiss LSM 710) and 40X water immersion objective lens (LDC-Apochromat 40×/1.1). Z stacks were collected at a scanning resolution of 1024 × 1024 pixels with a 0.5 μm Z-step increment size, and a Kalman averaging of 2–4. To obtain the location of individual RGCs, images of the retinal halves were acquired at 5X using an epifluorescence microscope (Zeiss Axio Imager 2) equipped with an Axiocam HR camera, and were later stitched together into whole-retina, orientation-preserved images, using Adobe Photoshop software. Image stacks for other analyses were acquired using a laser scanning confocal microscope (Leica TCS LSP8). Image stacks for individual BC axon terminals and ribbons were acquired using a 63× oil immersion objective (NA 1.4) with a voxel size of 0.05 × 0.05 × 0.25 μm. To obtain the location of biolistic labeled RGCs, image tiles covering the whole-mount retina were acquired under a 20x oil objective (NA 0.75) and automatically stitched together using the tile scan function of the Leica acquisition software. The x-y resolution for each tile was 0.96–1.5 μm and z resolution was 4–5 μm. All other

images were acquired using 60× oil objective (NA 1.4) with a voxel size of 0.1 × 0.1 × 0.3 μm.

QUANTIFICATION AND STATISTICAL ANALYSIS

Analysis of retinal ganglion cells—Each flat whole mount retina was reconstructed into a standard spherical retina space using Retistruct R package (Bleckert et al., 2014; Sterratt et al., 2013). The locations of analyzed RGCs were represented as longitudes (nasal to temporal axis) and latitudes (dorsal to ventral axis) in this spherical space. For individual RGCs, their dendrites were skeletonized using Imaris (Bitplane). Manual corrections were made whenever necessary. For mapping all the PSD95 puncta on the dendritic arbor of RGCs, space surrounding the dendrites was masked to limit the search for potential puncta, and puncta were detected using Imaris (Bitplane). Manual corrections were made after automatic detection. Information for both skeletonized dendrites and identified PSD95 puncta was exported to MATLAB (MathWorks). Colocalization of PSD95 puncta with BC axons was assessed plane-by-plane in 2-D using a custom-written program in MATLAB (Okawa et al., 2014). When FP-expressing BCs (T1 and T4) did not cover the entire dendritic arbors of RGC imaged, a 2D mask was created manually to outline the area occupied by the labeled BC axon terminals. Only PSD95 puncta on the RGC dendrites within these areas were included in the colocalization analysis. Contacts within the areas of 48 and 51 T1 BCs within OFF and OFF-T RGCs (n = 6 RGCs each), respectively, were analyzed.

Quantification of bipolar cell arbor size and ribbon density—For quantification of T1 and T4 OFF BC axon arbor sizes, images were acquired in the middle of four quadrants (dorsal-temporal, dorsal-nasal, ventral-temporal and ventral-nasal) of each whole mount retina. Each image stack covered an area of 246 × 246 μm. Each axon's volume was segmented using the surface function of Imaris (Bitplane). Their axonal territory area was defined as the area of the convex hull of the Z projection of the segmented axonal arbor. For T2 OFF BC, locations of individual T2 OFF BCs was marked by identifying their axon stalks in whole mount retinas immunolabeled with Syt2 (Fox and Sanes, 2007). Voronoi domains were generated using the identified axon stalk positions using R package 'spatstat' (Baddeley et al., 2015). The axon arbor sizes were estimated by the sizes of voronoi domains. For measuring ribbon density on BC axon terminals, masks of individual BC terminals were generated using the Labelfield function in Amira (FEI). The ribbon signal within the bipolar axon terminals was isolated by multiplying the original image by the mask. The ribbons were detected by 'dot finding' functions in Imaris (Bitplane) with manual correction.

Statistics—All statistics were performed using R version 3.4.1 (R Foundation for Statistical Computing; https://www.R-project.org). Unless noted otherwise, a two-tailed Mann-Whitney test was used to compare two groups of samples. Kruskal-Wallis one way analysis of variance was performed for more than two sample groups. Significance was determined at $p < 0.05$. Data are presented as mean ± SEM.

Supplementary Material

Refer to Web version on PubMed Central for supplementary material.

ACKNOWLEDGMENTS

We would like to thank Kaori Oda and Mei Zhang for technical assistance and all the members from Wong lab for helpful discussions. We also thank Dr. Luca Della Santina for critical comments on the drafts. This work was supported by HFSP grant (to L.L., F.S., and R.O.L.W.), NIH U01NS090562 (to S. Seung, R.O.L.W., M. Meister, T. Euler, and A.D.H.), NIH EY01730 (to M. Neitz), and research grants from the German Research Community DFG (SFB894, TPA7, and Schm797/8-1 to F.S.).

REFERENCES

Asari H, and Meister M (2012). Divergence of visual channels in the inner retina. Nat. Neurosci 15, 1581–1589. [PubMed: 23086336]

Awatramani GB, and Slaughter MM (2000). Origin of transient and sustained responses in ganglion cells of the retina. J. Neurosci 20, 7087–7095. [PubMed: 10995856]

Baddeley A, Rubak E, and Turner R (2015). Spatial Point Patterns: Methodology and Applications with R (Chapman and Hall/CRC Press).

Bae JA, Mu S, Kim JS, Turner NL, Tartavull I, Kemnitz N, Jordan CS, Norton AD, Silversmith WM, Prentki R, et al.; Eyewirers (2018). Digital museum of retinal ganglion cells with dense anatomy and physiology. Cell 173, 1293–1306. e19.

Beier KT, Borghuis BG, El-Danaf RN, Huberman AD, Demb JB, and Cepko CL (2013). Transsynaptic tracing with vesicular stomatitis virus reveals novel retinal circuitry. J. Neurosci 33, 35–51. [PubMed: 23283320]

Berck ME, Khandelwal A, Claus L, Hernandez-Nunez L, Si G, Tabone CJ, Li F, Truman JW, Fetter RD, Louis M, et al. (2016). The wiring diagram of a glomerular olfactory system. eLife 5, e14859. [PubMed: 27177418]

Berntson A, and Taylor WR (2000). Response characteristics and receptive field widths of on-bipolar cells in the mouse retina. J. Physiol 524, 879–889. [PubMed: 10790165]

Bleckert A, Schwartz GW, Turner MH, Rieke F, and Wong RO (2014). Visual space is represented by nonmatching topographies of distinct mouse retinal ganglion cell types. Curr. Biol 24, 310–315. [PubMed: 24440397]

Callaway EM (2002). Cell type specificity of local cortical connections. J. Neurocytol 31, 231–237. [PubMed: 12815242]

Coombs JL, Van Der List D, and Chalupa LM (2007). Morphological properties of mouse retinal ganglion cells during postnatal development. J. Comp. Neurol 503, 803–814. [PubMed: 17570502]

Crook JD, Peterson BB, Packer OS, Robinson FR, Troy JB, and Dacey DM (2008). Y-cell receptive field and collicular projection of parasol ganglion cells in macaque monkey retina. J. Neurosci 28, 11277–11291. [PubMed: 18971470]

Cruz-Martı´n A, El-Danaf RN, Osakada F, Sriram B, Dhande OS, Nguyen PL, Callaway EM, Ghosh A, and Huberman AD (2014). A dedicated circuit links direction-selective retinal ganglion cells to the primary visual cortex. Nature 507, 358–361. [PubMed: 24572358]

Dacey DM (1993). The mosaic of midget ganglion cells in the human retina. J. Neurosci 13, 5334–5355. [PubMed: 8254378]

Della Santina L., Kuo SP, Yoshimatsu T, Okawa H, Suzuki SC, Hoon M, Tsuboyama K, Rieke F, and Wong ROL (2016). Glutamatergic monopolar interneurons provide a novel pathway of excitation in the mouse retina. Curr. Biol 26, 2070–2077. [PubMed: 27426514]

Demb JB, Haarsma L, Freed MA, and Sterling P (1999). Functional circuitry of the retinal ganglion cell's nonlinear receptive field. J. Neurosci 19, 9756–9767. [PubMed: 10559385]

Demb JB, Zaghloul K, Haarsma L, and Sterling P (2001). Bipolar cells contribute to nonlinear spatial summation in the brisk-transient (Y) ganglion cell in mammalian retina. J. Neurosci 21, 7447–7454. [PubMed: 11567034]

Dhande OS, Estevez ME, Quattrochi LE, El-Danaf RN, Nguyen PL, Berson DM, and Huberman AD (2013). Genetic dissection of retinal inputs to brainstem nuclei controlling image stabilization. J. Neurosci 33, 17797–17813. [PubMed: 24198370]

Dunn FA, and Wong RO (2012). Diverse strategies engaged in establishing stereotypic wiring patterns among neurons sharing a common input at the visual system's first synapse. J. Neurosci 32, 10306–10317. [PubMed: 22836264]

Dunn FA, and Wong RO (2014). Wiring patterns in the mouse retina: collecting evidence across the connectome, physiology and light microscopy. J. Physiol 592, 4809–4823. [PubMed: 25172948]

El-Danaf RN, and Huberman AD (2015). Characteristic patterns of dendritic remodeling in early-stage glaucoma: evidence from genetically identified retinal ganglion cell types. J. Neurosci 35, 2329–2343. [PubMed: 25673829]

El-Danaf RN, and Huberman AD (2018). Sub-topographic maps for regionally enhanced analysis of visual space in the mouse retina. J. Comp. Neurol, Published online April 20, 2018. 10.1002/cne.24457.

Enroth-Cugell C, and Robson JG (1966). The contrast sensitivity of retinal ganglion cells of the cat. J. Physiol 187, 517–552. [PubMed: 16783910]

Euler T, Haverkamp S, Schubert T, and Baden T (2014). Retinal bipolar cells: elementary building blocks of vision. Nat. Rev. Neurosci 15, 507–519. [PubMed: 25158357]

Fisxek M, and Wilson RI (2014). Stereotyped connectivity and computations in higher-order olfactory neurons. Nat. Neurosci 17, 280–288. [PubMed: 24362761]

Fox MA, and Sanes JR (2007). Synaptotagmin I and II are present in distinct subsets of central synapses. J. Comp. Neurol 503, 280–296. [PubMed: 17492637]

Franke K, Berens P, Schubert T, Bethge M, Euler T, and Baden T (2017). Inhibition decorrelates visual feature representations in the inner retina. Nature 542, 439–444. [PubMed: 28178238]

Freeman J, Field GD, Li PH, Greschner M, Gunning DE, Mathieson K, Sher A, Litke AM, Paninski L, Simoncelli EP, and Chichilnisky EJ (2015). Mapping nonlinear receptive field structure in primate retina at single cone resolution. eLife 4, e05241. [PubMed: 26517879]

Gollisch T (2013). Features and functions of nonlinear spatial integration by retinal ganglion cells. J. Physiol. Paris 107, 338–348. [PubMed: 23262113]

Hammond P (1974). Cat retinal ganglion cells: size and shape of receptive field centres. J. Physiol 242, 99–118. [PubMed: 4436829]

Helmstaedter M, Briggman KL, Turaga SC, Jain V, Seung HS, and Denk W (2013). Connectomic reconstruction of the inner plexiform layer in the mouse retina. Nature 500, 168–174. [PubMed: 23925239]

Hochstein S, and Shapley RM (1976). Linear and nonlinear spatial subunits in Y cat retinal ganglion cells. J. Physiol 262, 265–284. [PubMed: 994040]

Hoon M, Sinha R, Okawa H, Suzuki SC, Hirano AA, Brecha N, Rieke F, and Wong RO (2015). Neurotransmission plays contrasting roles in the maturation of inhibitory synapses on axons and dendrites of retinal bipolar cells. Proc. Natl. Acad. Sci. USA 112, 12840–12845. [PubMed: 26420868]

Huberman AD, Manu M, Koch SM, Susman MW, Lutz AB, Ullian EM, Baccus SA, and Barres BA (2008). Architecture and activity-mediated refinement of axonal projections from a mosaic of genetically identified retinal ganglion cells. Neuron 59, 425–438. [PubMed: 18701068]

Hughes S, Watson TS, Foster RG, Peirson SN, and Hankins MW (2013). Nonuniform distribution and spectral tuning of photosensitive retinal ganglion cells of the mouse retina. Curr. Biol 23, 1696–1701. [PubMed: 23954426]

Kaas JH, Nelson RJ, Sur M, Lin CS, and Merzenich MM (1979). Multiple representations of the body within the primary somatosensory cortex of primates. Science 204, 521–523. [PubMed: 107591]

Kerschensteiner D, Morgan JL, Parker ED, Lewis RM, and Wong RO (2009). Neurotransmission selectively regulates synapse formation in parallel circuits in vivo. Nature 460, 1016–1020. [PubMed: 19693082]

Knibestöl M, and Vallbo AB (1970). Single unit analysis of mechanoreceptor activity from the human glabrous skin. Acta Physiol. Scand 80, 178–195. [PubMed: 5475340]

Lee S, Zhang Y, Chen M, and Zhou ZJ (2016). Segregated glycine-glutamate co-transmission from vGluT3 amacrine cells to contrast-suppressed and contrast-enhanced retinal circuits. Neuron 90, 27–34. [PubMed: 26996083]

Lu Q, Ivanova E, and Pan ZH (2009). Characterization of green fluorescent protein-expressing retinal cone bipolar cells in a 5-hydroxytryptamine receptor 2a transgenic mouse line. Neuroscience 163, 662–668. [PubMed: 19589372]

Mataruga A, Kremmer E, and MÜller F (2007). Type 3a and type 3b OFF cone bipolar cells provide for the alternative rod pathway in the mouse retina. J. Comp. Neurol 502, 1123–1137. [PubMed: 17447251]

Morgan JL, Dhingra A, Vardi N, and Wong RO (2006). Axons and dendrites originate from neuroepithelial-like processes of retinal bipolar cells. Nat. Neurosci 9, 85–92. [PubMed: 16341211]

Morgan JL, Schubert T, and Wong RO (2008). Developmental patterning of glutamatergic synapses onto retinal ganglion cells. Neural Develop 3, 8.

Morgan JL, Soto F, Wong RO, and Kerschensteiner D (2011). Development of cell type-specific connectivity patterns of converging excitatory axons in the retina. Neuron 71, 1014–1021. [PubMed: 21943599]

Münch TA, da Silveira RA, Siegert S, Viney TJ, Awatramani GB, and Roska B (2009). Approach sensitivity in the retina processed by a multifunctional neural circuit. Nat. Neurosci 12, 1308–1316. [PubMed: 19734895]

Neumann S, HÜser L, Ondreka K, Auler N, and Haverkamp S (2016). Cell type-specific bipolar cell input to ganglion cells in the mouse retina. Neuroscience 316, 420–432. [PubMed: 26751712]

Niell CM (2015). Cell types, circuits, and receptive fields in the mouse visual cortex. Annu. Rev. Neurosci 38, 413–431. [PubMed: 25938727]

Okawa H, Della Santina L., Schwartz GW, Rieke F, and Wong RO (2014). Interplay of cell-autonomous and nonautonomous mechanisms tailors synaptic connectivity of converging axons in vivo. Neuron 82, 125–137. [PubMed: 24698272]

Olveczky BP, Baccus SA, and Meister M (2007). Retinal adaptation to object motion. Neuron 56, 689–700. [PubMed: 18031685]

Peters A, and Feldman ML (1976). The projection of the lateral geniculate nucleus to area 17 of the rat cerebral cortex. I. General description. J. Neurocytol 5, 63–84. [PubMed: 1249593]

Petrusca D, Grivich MI, Sher A, Field GD, Gauthier JL, Greschner M, Shlens J, Chichilnisky EJ, and Litke AM (2007). Identification and characterization of a Y-like primate retinal ganglion cell type. J. Neurosci 27, 11019–11027. [PubMed: 17928443]

Polyak SL (1941). The Retina (Illinois: The University of Chicago Press).

Roska B, and Werblin F (2001). Vertical interactions across ten parallel, stacked representations in the mammalian retina. Nature 410, 583–587. [PubMed: 11279496]

Rust NC, Schwartz O, Movshon JA, and Simoncelli EP (2005). Spatio-temporal elements of macaque v1 receptive fields. Neuron 46, 945–956. [PubMed: 15953422]

Sanes JR, and Masland RH (2015). The types of retinal ganglion cells: current status and implications for neuronal classification. Annu. Rev. Neurosci 38, 221–246. [PubMed: 25897874]

Schwartz G, and Rieke F (2011). Perspectives on: information and coding in mammalian sensory physiology: nonlinear spatial encoding by retinal ganglion cells: when 1 + 1 s 2. J. Gen. Physiol 138, 283–290. [PubMed: 21875977]

Schwartz GW, Okawa H, Dunn FA, Morgan JL, Kerschensteiner D, Wong RO, and Rieke F (2012). The spatial structure of a nonlinear receptive field. Nat. Neurosci 15, 1572–1580. [PubMed: 23001060]

Shaner NC, Lin MZ, McKeown MR, Steinbach PA, Hazelwood KL, Davidson MW, and Tsien RY (2008). Improving the photostability of bright monomeric orange and red fluorescent proteins. Nat. Methods 5, 545–551. [PubMed: 18454154]

Sterratt DC, Lyngholm D, Willshaw DJ, and Thompson ID (2013). Standard anatomical and visual space for the mouse retina: computational reconstruction and transformation of flattened retinae with the Retistruct package. PLoS Comput. Biol 9, e1002921. [PubMed: 23468609]

Stone C, and Pinto LH (1993). Response properties of ganglion cells in the isolated mouse retina. Vis. Neurosci 10, 31–39. [PubMed: 8424927]

Tien NW, Soto F, and Kerschensteiner D (2017). Homeostatic plasticity shapes cell-type-specific wiring in the retina. Neuron 94, 656–665. e4. [PubMed: 28457596]

Tsukamoto Y, and Omi N (2014). Some OFF bipolar cell types make contact with both rods and cones in macaque and mouse retinas. Front. Neuroanat 8, 105. [PubMed: 25309346]

van Wyk M, Wa¨ ssle H, and Taylor WR (2009). Receptive field properties of ON- and OFF-ganglion cells in the mouse retina. Vis. Neurosci 26, 297–308. [PubMed: 19602302]

Warwick RA, Kaushansky N, Sarid N, Golan A, and Rivlin-Etzion M (2018). Inhomogeneous encoding of the visual field in the mouse retina. Curr. Biol 28, 655–665. e3. [PubMed: 29456141]

Wäsle H, and Boycott BB (1991). Functional architecture of the mammalian retina. Physiol. Rev 71, 447–480. [PubMed: 2006220]

Wässle H, Puller C, MÜller F, and Haverkamp S (2009). Cone contacts, mosaics, and territories of bipolar cells in the mouse retina. J. Neurosci 29, 106–117. [PubMed: 19129389]

Wei W, Elstrott J, and Feller MB (2010). Two-photon targeted recording of GFP-expressing neurons for light responses and live-cell imaging in the mouse retina. Nat. Protoc 5, 1347–1352. [PubMed: 20595962]

Williams ME, de Wit J, and Ghosh A (2010). Molecular mechanisms of synaptic specificity in developing neural circuits. Neuron 68, 9–18. [PubMed: 20920787]

Zhang AJ, and Wu SM (2009). Receptive fields of retinal bipolar cells are mediated by heterogeneous synaptic circuitry. J. Neurosci 29, 789–797. [PubMed: 19158304]

Zhang Y, Kim IJ, Sanes JR, and Meister M (2012). The most numerous ganglion cell type of the mouse retina is a selective feature detector. Proc. Natl. Acad. Sci. USA 109, E2391–E2398. [PubMed: 22891316]

Zhang C, Kolodkin AL, Wong RO, and James RE (2017). Establishing wiring specificity in visual system circuits: from the retina to the brain. Annu. Rev. Neurosci 40, 395–424. [PubMed: 28460185]

Zipursky SL, and Sanes JR (2010). Chemoaffinity revisited: dscams, proto-cadherins, and neural circuit assembly. Cell 143, 343–353. [PubMed: 21029858]

Highlights

- Bipolar cells (BCs) and ganglion cells (GCs) can vary topographically in size
- Changes in BC size do not always scale with that of their postsynaptic GCs
- Proportion of synapses from each BC type with partner GC is invariant of location
- BC axonal tiling promotes maintenance of stereotypic BC-GC connectivity patterns

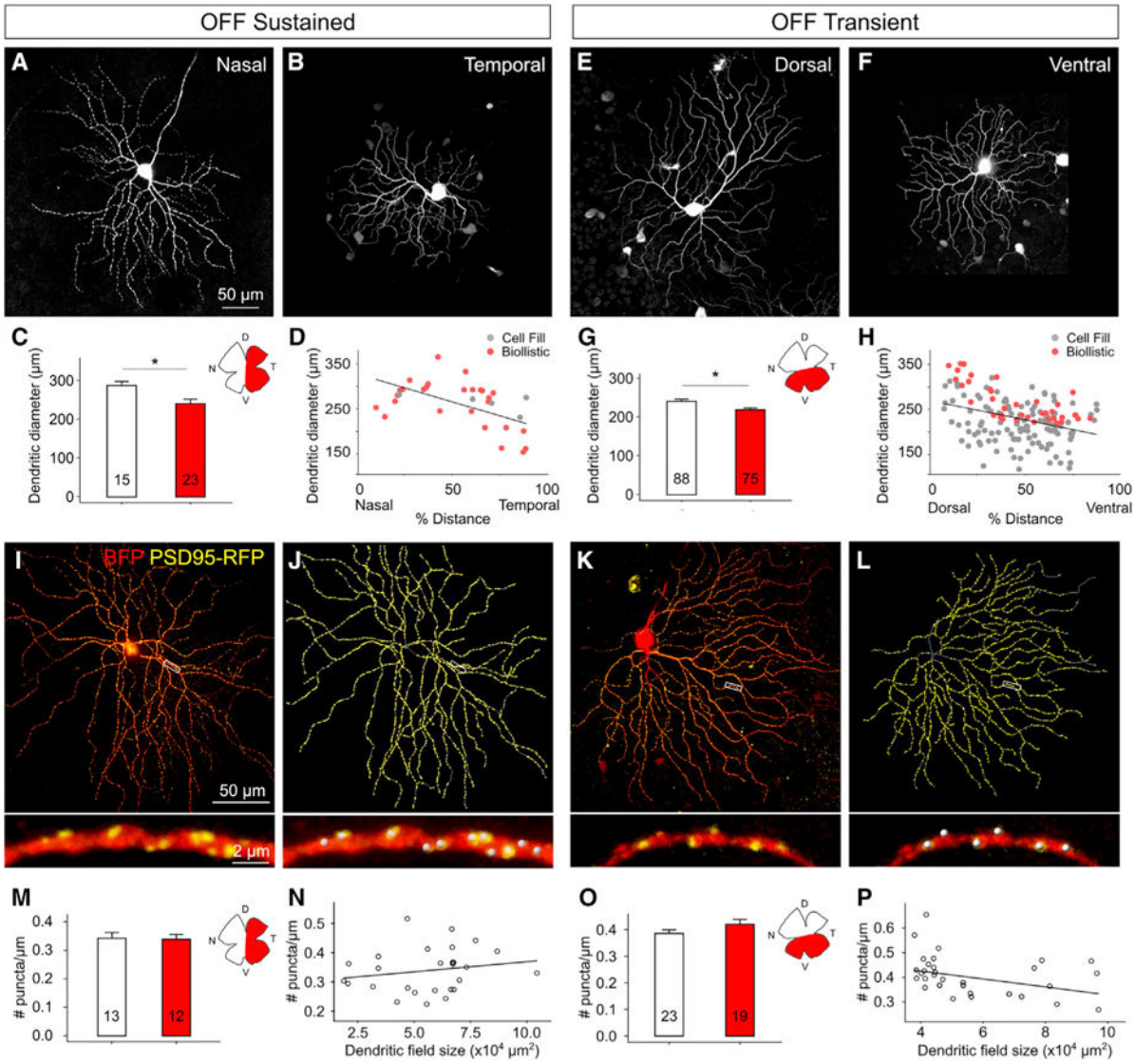

Figure 1. Dendritic Morphology and PSD95 Puncta Density of OFF-S and OFF-T RGCs across the Retina

(A and B) Single-cell morphology of OFF-S ganglion cells within the (A) nasal (N) or the (B) temporal (T) retina labeled by biolistic transfection.

(C) Average dendritic field size at different retinal locations; p = 0.012.

(D) Dendritic diameter as a function of percent distance along the N-T axis. Data collected in total from 12 biolistic transfected retinas and 4 dye-injected retinas are shown.

(E and F) Dendritic morphology for OFF-T RGCs in the (E) dorsal (D) or (F) ventral (V) retinas.

(G) Average dendritic diameters of OFF-T RGCs at different retinal locations; p = 0.007.

(H) Dendritic diameter as a function of percent distance along the D-V axis.(D and H) Regression line fitted to the pooled data. Data collected in total from 17 biolistic transfected retinas and 19 dye-injected retinas are shown.

(I–L) Whole-mount views of an OFF-S (I) and OFF-T (K) RGC biolistically labeled by BFP and PSD95-RFP and the respective distributions of PSD95 puncta across the arbors (J and

L). Magnified views of a stretch of dendrite (boxed regions) are shown in the lower panels of (I) and (K). PSD95-RFP puncta identified for quantification shown by gray dots (J and L, lower panels).

(M and O) Average linear density of PSD95 puncta for OFF-S (M) and OFF-T (O) at different retinal locations.

(N and P) Scatterplots show linear density of PSD95 puncta as a function of dendritic field size of OFF-S (N) and OFF-T (P).

Linear regression: OFF-S: $\beta = 6.890e{-}07$, $p = 0.348$, $r^2 = 0.04$; OFF-T: $b = -1.615e{-}06$, $p = 0.025$, $r^2 = 0.14$. * indicates $p < 0.05$ in (C) and (G). Error bars are SEM. See also Figure S4.

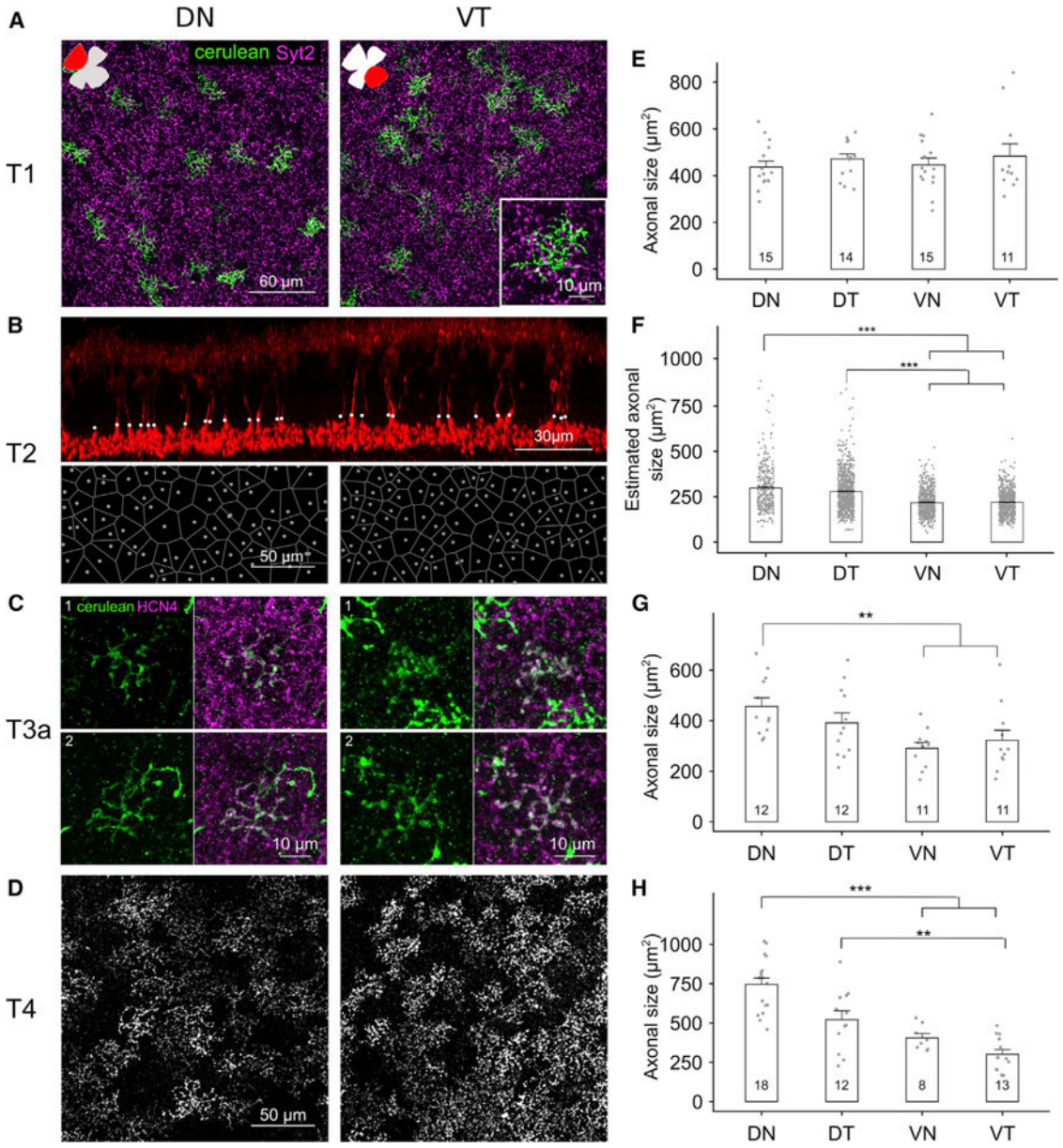

Figure 2. Variations in BC Axonal Size with Retinal Location

(A–D) BC axonal terminal sizes were determined using transgenic lines in which a single BC type expresses fluorescent protein (A, T1, *Vsx1-cerulean2*; C, T3a, *Vsx1-cerulean1*; D, T4, *5HTR2a-EGFP*) or estimated from their Voronoi domains based on their axon stalk positions (B, T2, white dots).

(E–H) Axonal sizes at four retinal locations are shown here for T1 (E), T2 (F), T3a (G), and T4 (H) bipolar cells.

D, dorso-nasal; DT, dorso-temporal; VN, ventro-nasal; VT, ventro-temporal. **$p < 0.001$; ***$p < 0.0001$. Numbers indicate number of cells from 2–5 retinas. Error bars are SEM. See also Figures S1 and S4.

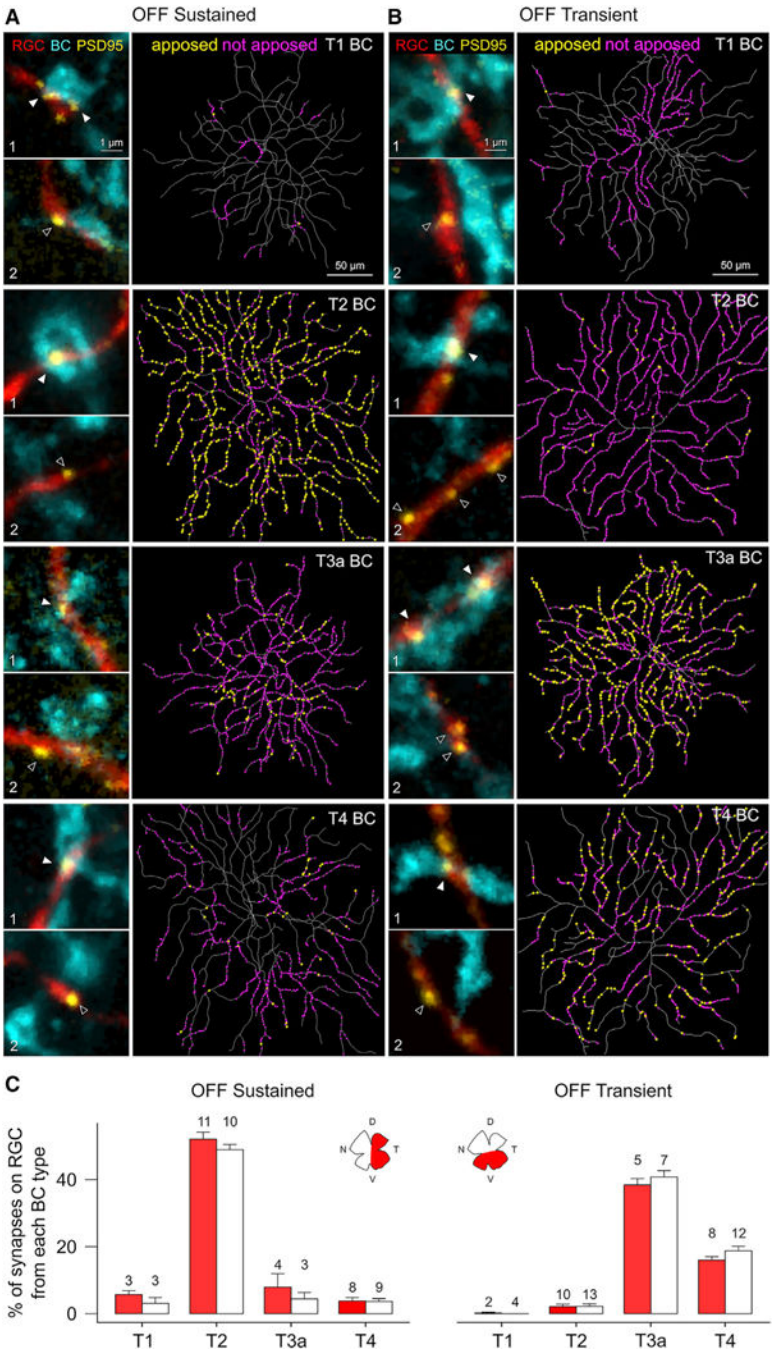

Figure 3. OFF-S and OFF-T Alpha RGCs Are Differentially Connected to 4 Types of OFF BCs

(A and B) Maps of PSD95-FP apposed (yellow dots) or not apposed (magenta dots) to axon terminals of each BC type are shown for OFF-S (A) or OFF-T alpha RGCs (B). Magnified views of an example of PSD95 (yellow) puncta on the RGC dendrite apposed (solid arrowhead, 1) or not apposed (open arrowhead, 2) to axon terminals of the BC are shown on the left. Because labeling of T1 and T4 BCs was not complete, we only determined the synaptic contacts on the dendritic segments of the RGCs within an area where BCs were labeled. Grey segments of the dendrites indicate regions where there were no labeled BCs.

(C) Quantification (mean ± SEM) showing the pro-portion of the total number of synapses on the dendritic arbor of OFF-S (left) and OFF-T (right) RGCs contributed by each BC type at different retinal locations. Number of cells in each region is provided.
See also Figures S2, S3, and S4.

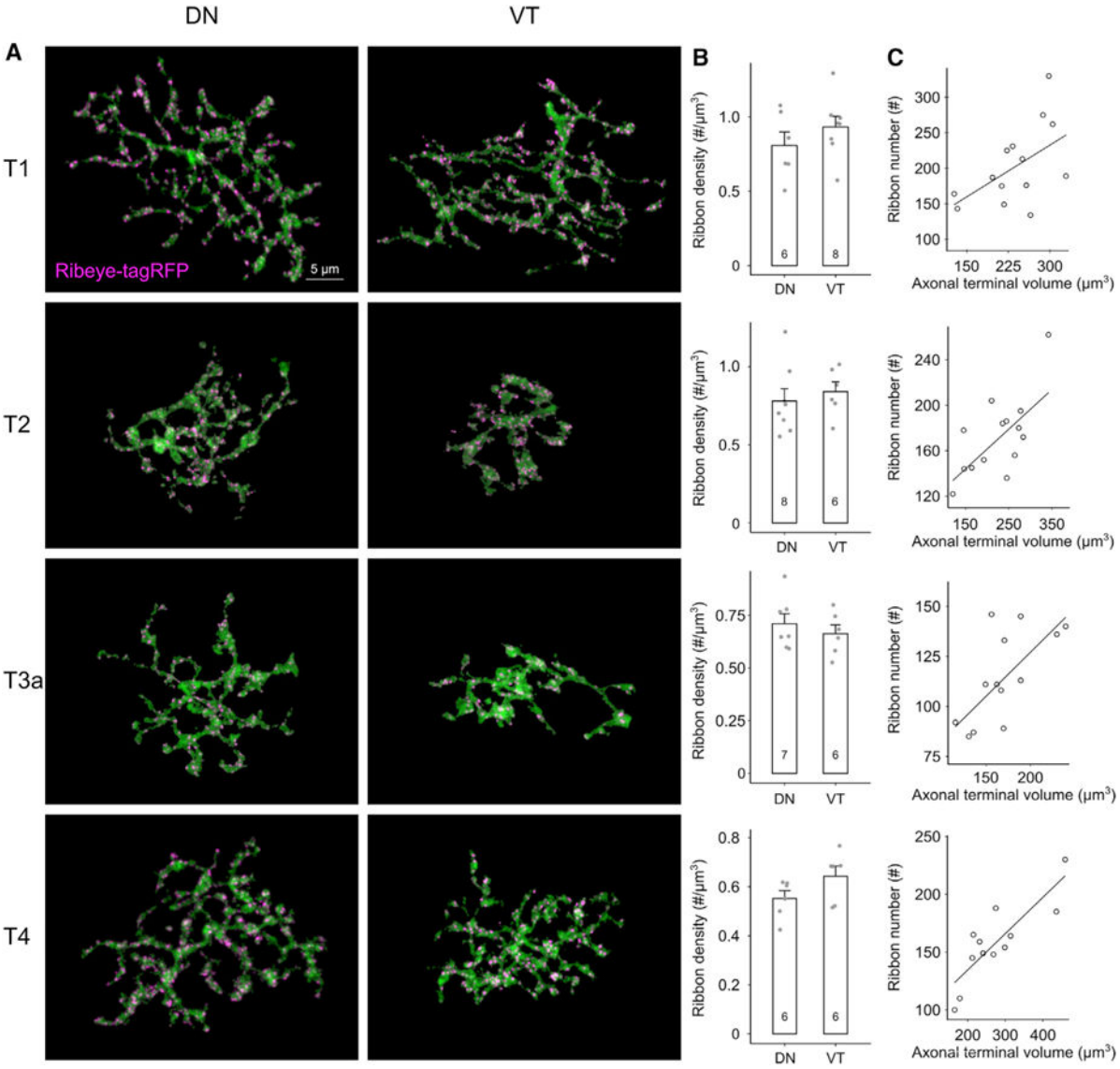

Figure 4. Ribbon Densities of 4 OFF BC Types Are Unchanged across the Retina

(A) Maximum intensity projections of confocal image stacks of isolated axon terminals and ribbons (*Ribeye-ribeye-tagRFP*) of four types of BCs at dorso-nasal (DN) and ventro-temporal (VT) locations.

(B) Quantification of ribbon density (mean ± SEM) per axon terminal at two retinal locations. Numbers indicate number of cells from 2–4 retinas.

(C) Scatterplot of ribbon number as a function of axon terminal volume. Solid lines represent linear regression lines. T1: $\beta = 0.5209$, $p = 0.039$, $r^2 = 0.2515$; T2: $\beta = 0.3761$, $p = 0.007$, $r^2 = 0.4671$; T3a: $p = 0.534$; $b = 0.4256$, $p = 0.0112$, $r^2 = 0.4078$; T4: $\beta = 0.3136$, $p < 0.001$, $r^2 = 0.6865$.

See also Figure S4.

REAGENT or RESOURCE	SOURCE	IDENTIFIER
Antibodies		
Mouse monoclonal anti-synaptotagmin II	Zebrafish International Resource	Cat# znp-1; RRID: AB_10013783
Rabbit polyclonal anti-HCN4	Alomone Labs	Cat# APC-052, RRID:AB_2039906
Chicken polyclonal anti-GFP	Abcam	Cat# ab13970, RRID:AB_300798
Mouse monoclonal anti-myc	DSHB	Cat# 9E 10, RRID:AB_2266850
Donkey polyclonal anti-chicken IgY, Alexa Fluor 488	Jackson ImmunoResearch Labs	Cat# 703-545-155, RRID: AB_2340375
Donkey polyclonal anti-rabbit IgG, Alexa Fluor 647	Jackson ImmunoResearch Labs	Cat# 711-605-152, RRID: AB_2492288
Goat anti-mouse IgG2a, Alexa Fluor 647	Jackson ImmunoResearch Labs	Cat# 115-605-206, RRID: AB_2338917
Goat anti-mouse IgG1, DyLight 405	Jackson ImmunoResearch Labs	Cat# 115-477-185, RRID: AB_2632529
Chemicals, Peptides, and Recombinant Proteins		
Alexa Fluor 555 hydrizide	Invitrogen	Cat# A20501MP
Normal Donkey Serum	Sigma-Aldrich	Cat# D9663
Vectashield	Vector Laboratories	Cat# H-1000, RRID: AB_2336789
Gold Particles/micro carriers (1.6 μm diameter)	Bio-Rad	Cat# 165-2264
Experimental Models: Organisms/Strains		
Mouse model: Vsx1-cerulean2	This paper	N/A
Mouse model: Vsx1-cerulean1	(Hoon et al., 2015)	N/A
Mouse model: Ribeye-ribeye-tagRFP	This paper	N/A
Mouse model: CB2-GFP	(Huberman et al., 2008)	RRID:MMRRC_000283-MU
Mouse model: 5HTR2a-EGFP	(Lu et al., 2009)	RRID:MMRRC_010915-UCD
Mouse model: Grm6-tdTomato	(Kerschensteiner et al., 2009)	N/A
Mouse model: Gus8.4-GFP	The Jackson Laboratory	RRID: IMSR_JAX:026704
Recombinant DNA		
Plasmid: pCMV-CFP	(Morgan et al., 2011)	N/A
Plasmid: pCMV-tagBFP2-myc	This paper (Modified from pEGFP-N1 from Clonetech)	N/A
Plasmid: pCMV-PSD95-tagRFP	This paper (Modified from pCMV-PSD95-YFP)	N/A
Plasmid: pCMV-PSD95-YFP	A.M.Craig, University of British Columbia (Morgan et al., 2008)	N/A
Software and Algorithms		
ImageJ	NIH	https://imagej.nih.gov/ij/, RRID: SCR_003070
Amira	Thermo-Fisher Scientific	https://www.fei.com/software/amira-avizo/, RRID: SCR_014305
Imaris	Bitplane	http://www.bitplane.com/, RRID: SCR_007370

REAGENT or RESOURCE	SOURCE	IDENTIFIER
MATLAB	MathWorks	https://www.mathworks.com/products/matlab.html, RRID: SCR_001622
R	R Core Team	https://www.r-project.org/, RRID:SCR_001905